Multifunctional "Add-On" Module Enabled NIR-II Imaging-Guided Synergistic Photothermal and Chemotherapy of Drug-Resistant Lung Cancer

Yu Li,[||] Qiang Zhu,[||] Pei He,[||] Tingjuan Wu, Zhen Ouyang, Lijun Zhu, Fang Wang, Xin Zhou, Zhong-Xing Jiang,* and Shizhen Chen*

Cite This: ACS Appl. Mater. Interfaces 2024, 16, 67275−67288

Read Online

ACCESS | Metrics & More | Article Recommendations | Supporting Information

ABSTRACT: Imaging-guided chemo-photothermal combination therapy (chemo-PTT) is recognized for its synergistic therapeutic effects, reduced side effects, and minimal drug resistance, while the development of such theranostics has been hampered by poor imaging and therapy performance and tedious formulation. Herein, we introduce an all-in-one "add-on" module (**BBT-C6**) for the convenient construction of doxorubicin (DOX)-loaded nanoparticles (DOX@BBT) and efficient second near-infrared (NIR-II) fluorescence imaging (FLI)-guided synergistic chemo-PTT of drug-resistant lung cancer. The delicate Janus amphiphilic structure of **BBT-C6** enables multifunctionality, including NIR-II FLI, aggregation-induced emission (AIE) characteristics, moderate photothermal conversion efficiency (PCE), excellent photostability, and polyethylene glycolation (PEGylation), which could improve the NIR-II FLI and PTT performance, relieve the complexity in theranostics, and enable high reproducibility of the multifunctional theranostics. Confocal microscopy revealed that **BBT@DOX** efficiently delivers DOX into cells, resulting in an increased accumulation of DOX that exceeds the efflux capacity of DOX-resistant cells. Both in vitro and in vivo studies demonstrate that **BBT-C6** enhances the effectiveness of **BBT@DOX**, achieving highly effective photothermal-chemo synergistic therapy against DOX-resistant lung cancer. Beyond developing a versatile "add-on" module for conveniently constructing multifunctional nanosystems, this study provides new insights into the design of advanced theranostics for precise biomedical applications.

Multifunctional "Add-on" Module

KEYWORDS: NIR-II fluorescent dyes, photothermal therapy, self-assembly, drug resistance, benzobisthiadiazole

1. INTRODUCTION

Photothermal therapy (PTT), which utilizes photothermal agents to absorb light and generate local temperature increases, has attracted considerable attention in cancer treatment due to its minimally invasive nature, high efficiency, and spatiotemporal selectivity. To achieve effective PTT, it is crucial to precisely localize tumors and confirm the accumulation of photothermal agents in tumors using imaging technology.[1−3] For this purpose, theranostics combining PTT with imaging capabilities are highly preferred. Fluorescence imaging (FLI) is a powerful tool for tumor localization and theranostic tracking due to its convenience, high sensitivity, and excellent spatial and temporal resolution.[4−6] Second near-infrared (NIR-II) FLI (1000−1700 nm) stands out as a valuable imaging technology due to its deep tissue penetration and low tissue autofluorescence.[7−9] Among the existing NIR-II fluorophores, organic types show promising prospects due to their biocompatibility, superior metabolic behavior, structural versatility, and easy processability. In addition, the optical properties can be fine-tuned by engineering the chemical structures.[10−13] However,

the application of most NIR-II fluorescent dyes in theranostics is hampered by low PTT performance and low fluorescence quantum yield (Φ) in aqueous media due to the aggregation-caused fluorescence quenching (ACQ) effect. Therefore, there is significant interest in developing aggregation-induced emission (AIE) NIR-II organic fluorophores with high Φ and PTT efficiency.[14−19]

On the therapy side, PTT has proven promising for cancer treatment because cancer cells typically exhibit low tolerance to temperature elevation. However, the therapeutic efficacy of PTT alone is usually compromised by the limited penetration depth of light, resulting in incomplete tumor eradication. Combining PTT with other treatment modalities such as
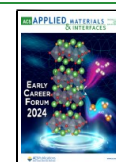
Scheme 1. Schematic Illustration of DOX-Loaded Nanoparticles (DOX@BBT), which was Self-Assembled from the Amphiphile BBT-C6, Soybean Phospholipid S95, and Pluronic F68, and DOX, for NIR-II FLI-Guided Synergistic Chemo-PTT of Drug-Resistant Lung Cancer
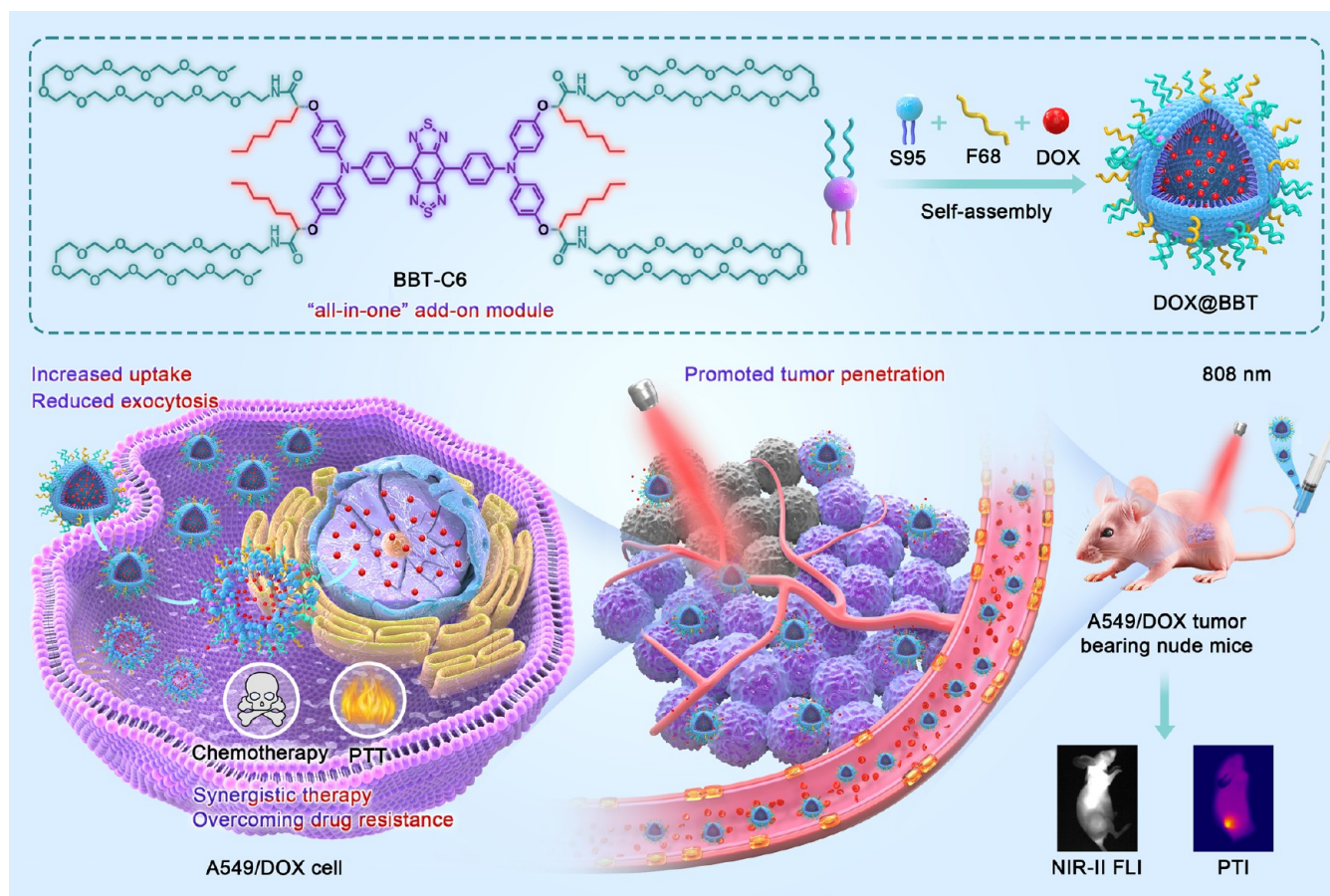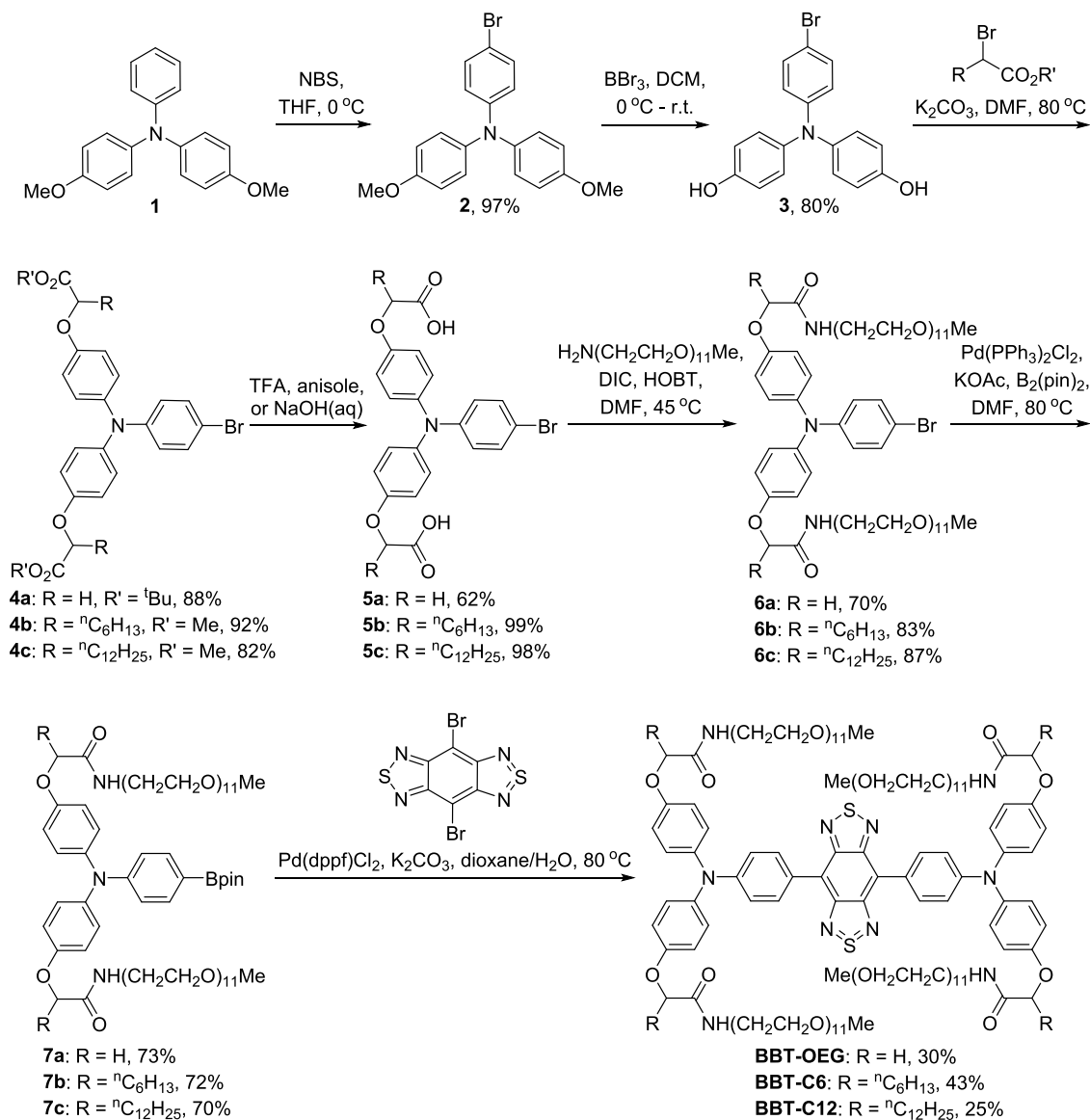

chemotherapy offers a more effective approach.[20−23] The local temperature elevation during PTT has been shown to increase the permeability of blood vessels, cell membranes, and extracellular matrix, thereby improving the uptake and penetration of chemotherapy agents into tumors, and improving the therapeutic efficacy against drug-resistant cancers.[24−27] Therefore, developing a comprehensive theranostic platform for NIR-II FLI-guided chemo-PTT is highly desirable. However, its development and clinical potential are severely hampered by the challenges of rational and effective incorporation of multiple components, including a NIR-II dye, a chemotherapy drug, formulation agents (such as phospholipids, polyethylene glycolation (PEGylation) agents, occasionally a biocompatible coating, and other additives), which lead to tedious formulation, poor reproducibility, and safety concerns associated with the complexity of its ingredients.[28−31] To address this challenge, versatile all-in-one "add-on" modules with precise chemical structures and multiple functions, such as self-assembly capability, NIR-II FLI, and PTT, are attractive, albeit challenging, for the convenient construction of multifunctional theranostics.[32−35]

Herein, a Janus macromolecular amphiphile (denoted as **BBT-C6**) featuring high AIE NIR-II fluorescence, a PCE of 37.9%, and excellent photostability was developed for self-assembly into DOX-loaded nanoparticles (DOX@BBT), thus serving as an all-in-one "add-on" module for convenient multifunctionalization of theranostics for NIR-II FLI-guided

chemo-photothermal therapy of drug-resistant lung cancer (Scheme 1). In **BBT-C6**, benzobisthiadiazole (BBTD) with two triphenylamines, a widely used planar donor−acceptor− donor (D−A−D) type NIR-II fluorophore, was employed as the NIR-II FL emitter, PTT agent, and scaffold for amphiphilic side chains. Four amphiphilic side chains with a hydrophobic 1-hexyl and a hydrophilic monodisperse oligo(ethylene glycol) (M-OEGs) were symmetrically introduced to four donor phenyl groups of the scaffold, which tuned the aggregation mode and restrained the intramolecular motions of the D−A− D structure for a delicate balance between AIE-type NIR-II fluorescence emission and photothermal conversion. Additionally, M-OEGs were employed to improve the water solubility and biocompatibility of **BBT-C6**, and, more importantly, facilitate the PEGylation of DOX@BBT for higher in vivo stability, longer blood circulation time, and better tumor targeting. After diagnostic NIR laser irradiation, the NIR-II FL of **BBT-C6** enabled accurate tumor localization and evaluation of tumor accumulation of **BBT@DOX** in vivo, thereby optimizing the timing of therapeutic laser irradiation. Meanwhile, real-time photothermal imaging guides laser power and duration optimization. To demonstrate the efficacy against drug resistance, assays on cytotoxicity, cellular uptake, and penetration ability into tumor spheroids were performed. Finally, antitumor studies on nude mice bearing xenograft A549 or A549/DOX lung tumors showed promising synergistic effects of PTT and chemotherapy, representing a

Scheme 2. Synthesis of Janus NIR-II Fluorescent Amphiphiles BBT-OEG, BBT-C6, and BBT-C12

4a: R = H, R' = ^{t}Bu, 88%
4b: R = ^{n}C$_6$H$_{13}$, R' = Me, 92%
4c: R = ^{n}C$_{12}$H$_{25}$, R' = Me, 82%

5a: R = H, 62%
5b: R = ^{n}C$_6$H$_{13}$, 99%
5c: R = ^{n}C$_{12}$H$_{25}$, 98%

6a: R = H, 70%
6b: R = ^{n}C$_6$H$_{13}$, 83%
6c: R = ^{n}C$_{12}$H$_{25}$, 87%

7a: R = H, 73%
7b: R = ^{n}C$_6$H$_{13}$, 72%
7c: R = ^{n}C$_{12}$H$_{25}$, 70%

BBT-OEG: R = H, 30%
BBT-C6: R = ^{n}C$_6$H$_{13}$, 43%
**BBT-C12**: R = ^{n}C$_{12}$H$_{25}$, 25%

promising strategy for the treatment of drug-resistant A549/DOX lung cancer.

2. RESULTS AND DISCUSSION

2.1. Synthesis and Characterization of BBTD-Based Amphiphilic Dyes. First, **BBT-C6**, along with a hydrophilic control BBT-OEG and a hydrophobic control BBT-C12, were conveniently synthesized on multihundred-milligram scales (Scheme 2). Commercially available 4,4′-dimethoxytriphenylamine **1** was first para-brominated with *N*-bromosuccinimide (NBS) and then demethylated with boron tribromide to give phenol **3**,[36] which was then alkylated with a series of α-brominated esters to give the corresponding esters **4a−c** in high yields over three steps. After removal of the protecting group in esters **4a−c**, the resulting acids **5a−c** were coupled with monodisperse methylated undeca(ethylene glycol) amine to give the corresponding amides **6a−c**, which were respectively converted to borates **7a−c** by the Miyaura boronation reaction.[37] After a series of catalyst and base screenings, **BBT-C6**, BBT-OEG, and BBT-C12 were prepared by Suzuki coupling reaction between borates **7a−c** and

commercially available 4,8-dibromobenzo[1,2-*c*:4,5-*c*′]bis-([1,2,5] thiadiazole) using Pd(dppf)Cl$_2$ as the catalyst and potassium acetate as the base.[38] The structures of the BBTs and their intermediates have been fully characterized by ^{1}H/^{13}C nuclear magnetic resonance (NMR) and mass spectra (Supporting Information).

Then, the effect of introducing 4 alkyl side chains on the physicochemical properties was comparatively investigated. First, BBT-OEG and **BBT-C6** have good water solubilities of about 10 and 5 mg/mL, respectively, while BBT-C12 has a poor water solubility, indicating that the water solubility decreased significantly with the length of the hydrophobic side chains. The *n*-octanol−water partition coefficients (Log *P*)[39] also showed that the lipophilicity of BBT-OEG, **BBT-C6**, and BBT-C12 increased with the length of the alkyl side chains (Figures 1a and S1). The poor water solubility and high lipophilicity of BBT-C12 excluded it from the downstream study. Second, compared to BBT-OEG, **BBT-C6** with hexyl side chains showed a slight red-shift of the maximum near-infrared (NIR) absorption at 746 nm (Figure 1b), a blue-shift of the maximum NIR-II FL emission at 1056 nm (Figure 1c),
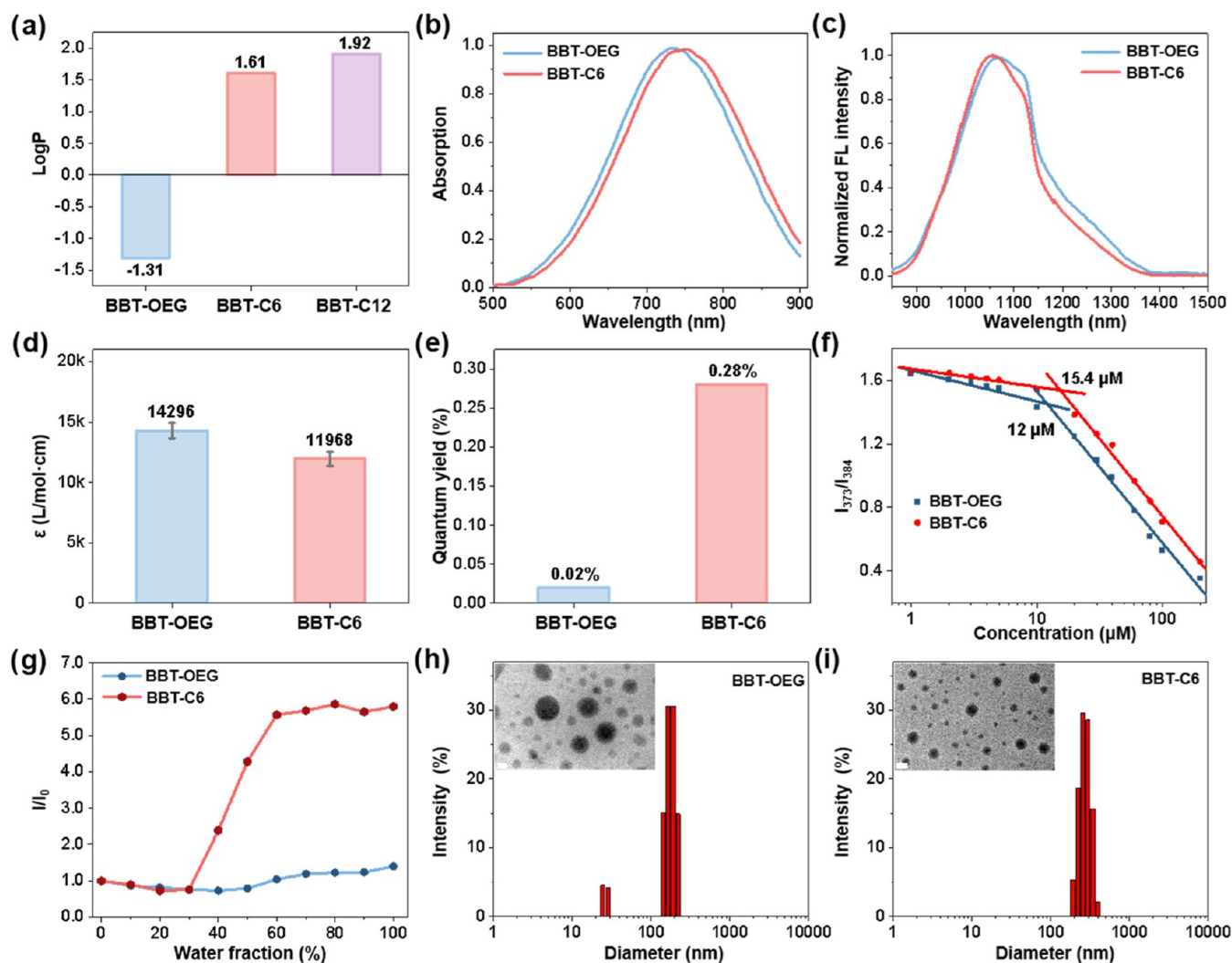
Figure 1. Log P of BBT-OEG, **BBT-C6**, and BBT-C12 (a). Visible-near infrared (Vis-NIR) absorption spectra (b), Vis-NIR-II FL emission spectra (c), molar extinction coefficient (d), fluorescence quantum yield (e), CMC (f), and solvent-dependent maximum NIR-II FL intensity (g) of BBT-OEG and **BBT-C6** in water. DLS with inserted TEM images of BBT-OEG (h) scale bar: 200 nm and **BBT-C6** (i) scale bar: 500 nm.

and a reduced molar extinction coefficient (ε) in water (Figures 1d and S2). Notably, the hexyl side chains in **BBT-C6** significantly promoted the absolute fluorescence quantum yield (Φ), resulting in a 24-fold enhancement compared to BBT-OEG as measured by a steady-state photoluminescence spectrometer (Figure 1e). Third, BBT-OEG and **BBT-C6** have a high tendency to aggregate in water with critical micelle concentrations (CMC)[40] of 12.0 and 15.4 μM, respectively (Figure 1f). When the solvent was gradually changed from methanol to water, the intensity ratio of the maximum NIR-II FL emission of BBT-OEG remained stable, while that of **BBT-C6** abruptly increased above 30% water, showing a high AIE effect of **BBT-C6** with a 5.7-fold increase in FL intensity (Figures 1g and S3). The rather similar CMCs and quite different solvent-dependent NIR-II FL of BBT-OEG and **BBT-C6** suggested different aggregation modes induced by the hexyl side chains. The hydrophobic hexyl side chains promoted a more homogeneous aggregation of **BBT-C6** compared to BBT-OEG as shown by dynamic light scattering (DLS) and transmission electron microscopy (TEM) images (Figures 1h,i and S4). Therefore, compared to BBT-OEG with a typical hydrophilic NIR-II dye structure, the 4 hexyl side chains in **BBT-C6** resulted in a negligible effect on the NIR absorption

and NIR-II FL emission, but significantly improved the fluorescence quantum yield and AIE effect (Table S1). Given the widespread use of OEG side chains to enhance the solubility of BBTD-based NIR-II FL agents,[41−44] incorporating amphiphilic side chains with OEG and alky chains could be an effective strategy to simultaneously improve the solubility, fluorescence quantum yield, and AIE efficacy.

2.2. Formulation and Characterization of BBT@DOX. With its desirable physicochemical properties, **BBT-C6** was selected as an "add-on" module[45−48] for the construction of theranostic nanoparticles. First, the photostability of **BBT-C6** in water was investigated. The maximum absorption intensity of **BBT-C6** showed minimal change after 60 min of 808 nm laser irradiation at 1.0 W/cm², while that of the commercial photothermal agent indocyanine green (ICG) decreased by 80% under the same conditions (Figure 2a), indicating the high photostability of **BBT-C6**. As shown in Figure 2b, the photothermal effect is positively related to the concentration of **BBT-C6** upon 808 nm laser irradiation (1.0 W/cm²). As the concentration increases to 100 μM, the temperature reaches a maximum of 74 °C, corresponding to a 52 °C temperature increase (ΔT) after 10 min of 808 nm laser irradiation (1.0 W/cm²), which is higher than that of BBT-OEG (ΔT = 45 °C)
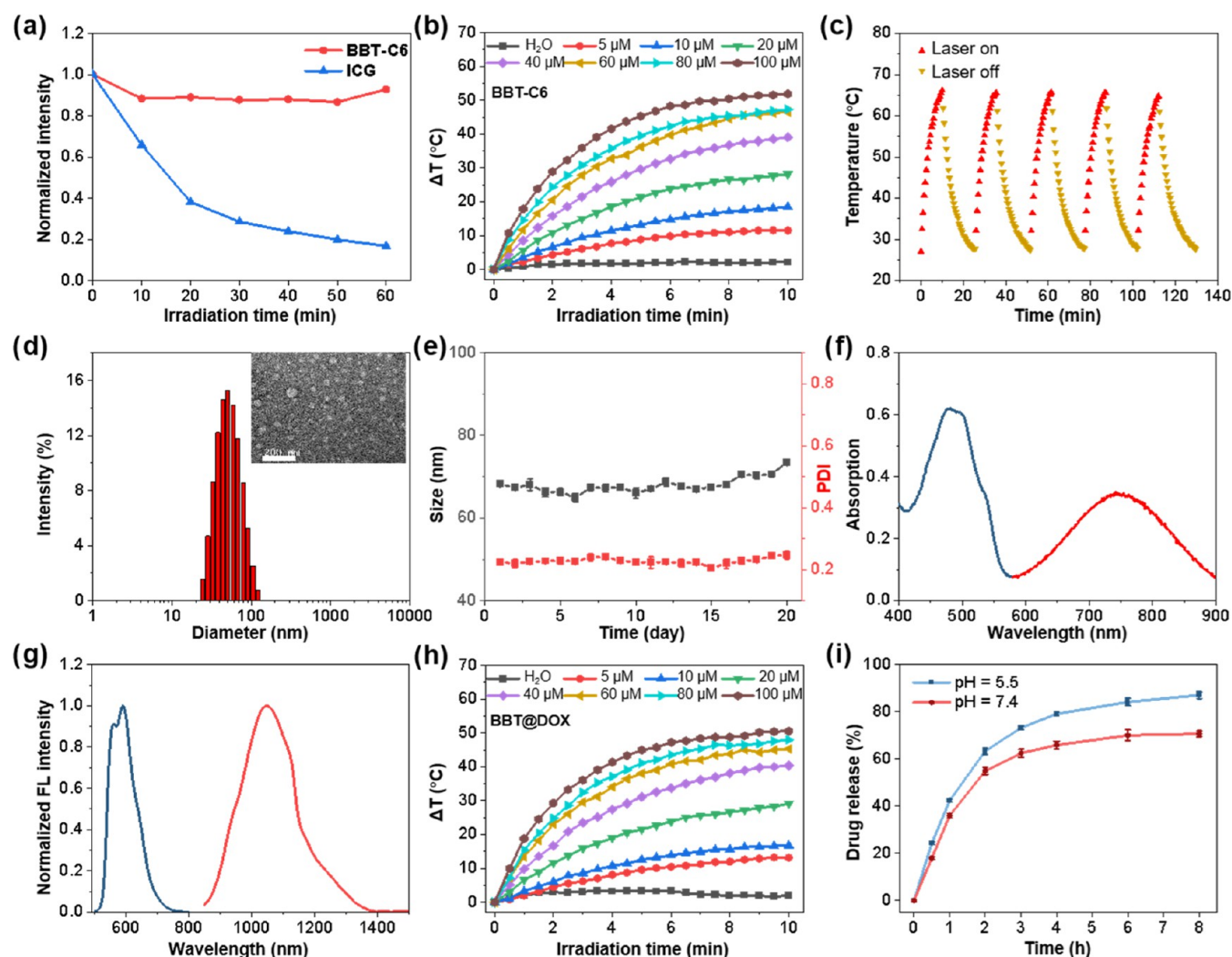
Figure 2. Laser irradiation time-dependent maximum absorption intensity of **BBT-C6** and ICG (a) and temperature changes of **BBT-C6** at various concentrations (b). Temperature changes of a 40 μM of **BBT-C6** solution with five cycles of laser irradiation and cooling (c). DLS with insert TEM image of **BBT@DOX** (d, scale bar 200 nm). Particle size and PDI of **BBT@DOX** in PBS over 20 days (e). The Vis-NIR absorption spectra (f) and Vis-NIR-II FL emission spectra (g) of **BBT@DOX**. Laser irradiation time-dependent temperature changes of **BBT@DOX** at various concentrations (h). DOX release curves of **BBT@DOX** under the indicated conditions (i). 808 nm laser irradiation at 1.0 W/cm^2 was used in all cases.

(Figure S5a). Furthermore, the PCE of **BBT-C6** in aqueous solution under 808 nm irradiation was calculated to be 37.9%, higher than that of ICG (33.1%)[49] and BBT-OEG (36.2%) (Figure S5b,c). The higher maximum photothermal temperature and better photothermal conversion efficiency of **BBT-C6** than BBT-OEG may be attributed to the hexyl side chains, which permit intramolecular motion that facilitates the nonradiative decay pathway in the aggregate state.[50,51] Notably, the PCE of **BBT-C6** is comparable to most organic photothermal agents with NIR-II fluorescence (Figure S5d). Moreover, the high photothermal stability of **BBT-C6** was demonstrated by five cycles of repeated laser irradiation and cooling, with the highest temperature of 65 °C consistently achieved (Figure 2c). As a result, the high and stable photothermal performance of **BBT-C6** makes it a promising agent for photothermal therapy. **BBT-C6** was then formulated with the chemotherapy drug doxorubicin (DOX) using the thin-film dispersion method with soybean phospholipid S95 and Pluronic F68 as surfactants, which provided a monodisperse nanoemulsion **BBT@DOX** with an average particle size of approximately 67 nm and a polydispersity index (PDI) of 0.22, as measured by DLS. Besides, **BBT@DOX** exhibited a nearly neutral surface charge, with a zeta potential of −0.1 mV (Figure S6a). This neutral charge is expected to minimize the adsorption of serum proteins.[52] The uniform spherical morphology and size of **BBT@DOX** were further confirmed by TEM images, showing an average diameter of 36 nm (Figures 2d and S6b). To demonstrate the reproducibility of **BBT@DOX** preparation, we conducted five batches at different times and by different individuals, all yielding consistent particle sizes and low PDIs, according to DLS results (Figure S6c,d). It is noteworthy that **BBT@DOX** showed high colloidal stability, with no apparent change in the average particle size and PDI over 20 days (Figure 2e). These findings underscore the superiority of the **BBT@DOX** formulation. The characteristic Vis-NIR absorption (Figure 2f) and Vis-NIR-II FL emission (Figure 2g) spectra of DOX (blue line) and **BBT-C6** (red line) in **BBT@DOX** confirmed the successful formulation, allowing a temperature increase similar to that of **BBT-C6** after laser irradiation (Figure 2h).
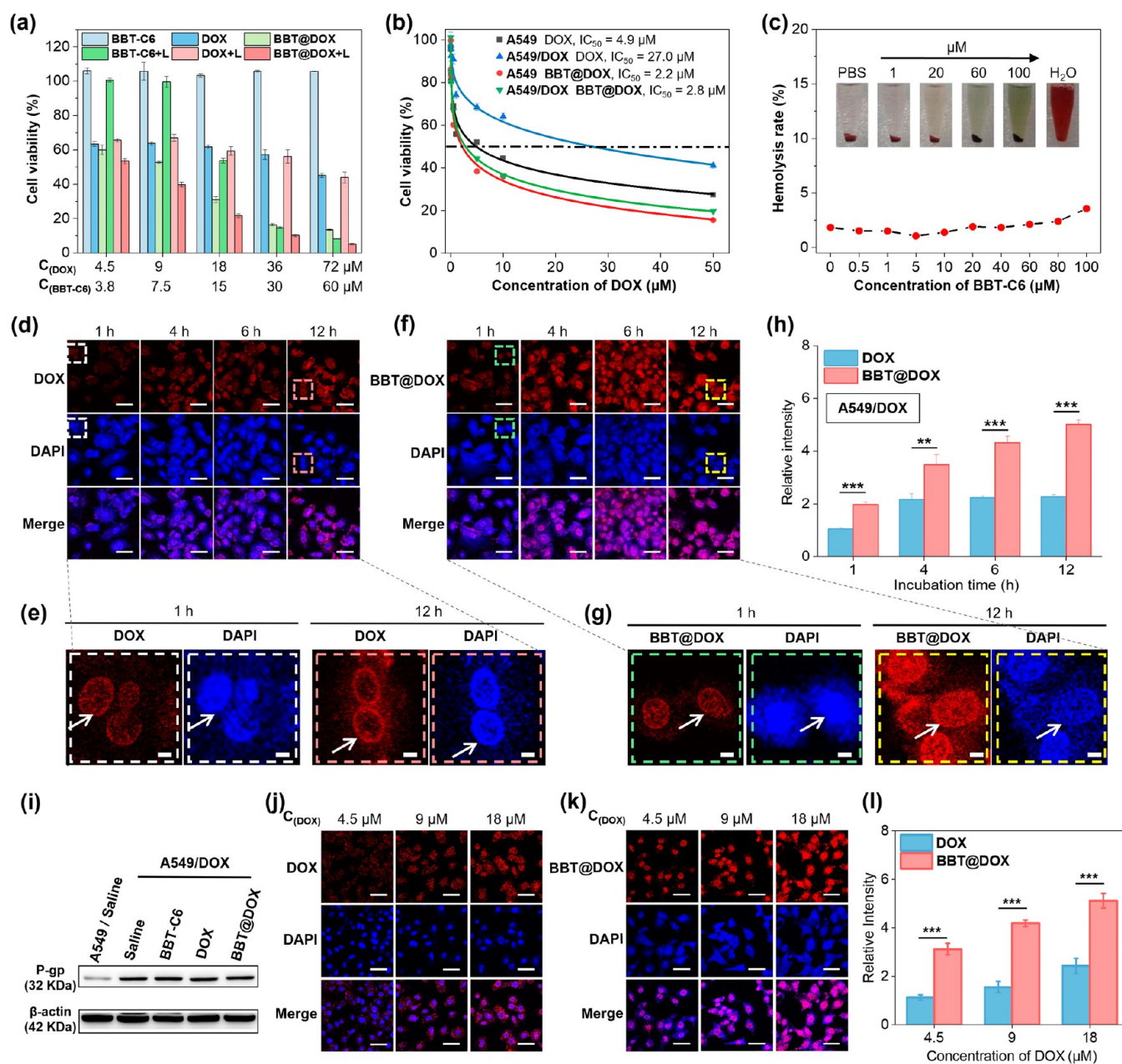
Figure 3. Cytotoxicity assay of **BBT-C6**, DOX, and **BBT@DOX** against A549/DOX cells (a, Data were expressed as means ± standard deviation (n = 3), 808 nm laser irradiation at 1.0 W/cm^2 was used). Inhibition curves and calculated IC$_{50}$ of DOX and **BBT@DOX** toward A549 cells and A549/DOX cells (b). Hemolysis assay of **BBT@DOX** with PBS and deionized water as controls (c). Confocal microscope images of DOX- and **BBT@DOX**-treated A549/DOX cells (d, f, scale bar: 50 μm), the magnified images of the nucleus of treated A549/DOX cells (e). DOX (g, **BBT@DOX**, scale bar: 6 μm), and their quantitative analysis (h). Western blot analysis of A549 and A549/DOX cells under different treatments as indicated (i). Confocal microscope images of A549/DOX cells treated with DOX and BBT@DOX (j, k, scale bar: 50 μm), and their quantitative analysis (l). The asterisks indicate the statistical significance, **p < 0.01, and ***p < 0.001.

The DOX encapsulation efficiency was measured at 97.1% with a drug loading content of 0.92%. Importantly, **BBT@DOX** achieved a slow DOX release of 60% over 8 h in a normal physiological medium (pH 7.4) and an enhanced release of about 90% DOX in a tumor microenvironment-like medium (pH 5.5), probably due to the protonation of DOX under acidic conditions (Figure 2i), which was highly preferred for tumor-targeted drug delivery. Therefore, a stable, monodisperse nanoemulsion **BBT@DOX**, characterized by high encapsulation efficiency and a sustained drug release profile, was successfully developed as an advanced multifunc-

tional platform for NIR-II FL imaging, PTT, and chemotherapy.

2.3. Cytotoxicity and Cellular Uptake of BBT@DOX. Following, the in vitro antitumor efficacy of **BBT@DOX** was evaluated in a panel of cells using the cell counting kit-8 (CCK-8) assay, including lung cancer A549 cells, doxorubicin-resistant A549/DOX cells, and human lung epithelial BEAS-2B cells. **BBT-C6** showed over 80% viability in the above cells at a high concentration of 64 μM, with viability dropping to less than 50% at 15 μM after laser irradiation (Figure S7a,b), indicating its low dark cytotoxicity and high phototherapy efficiency. Compared to DOX, **BBT@DOX** exhibited sig-
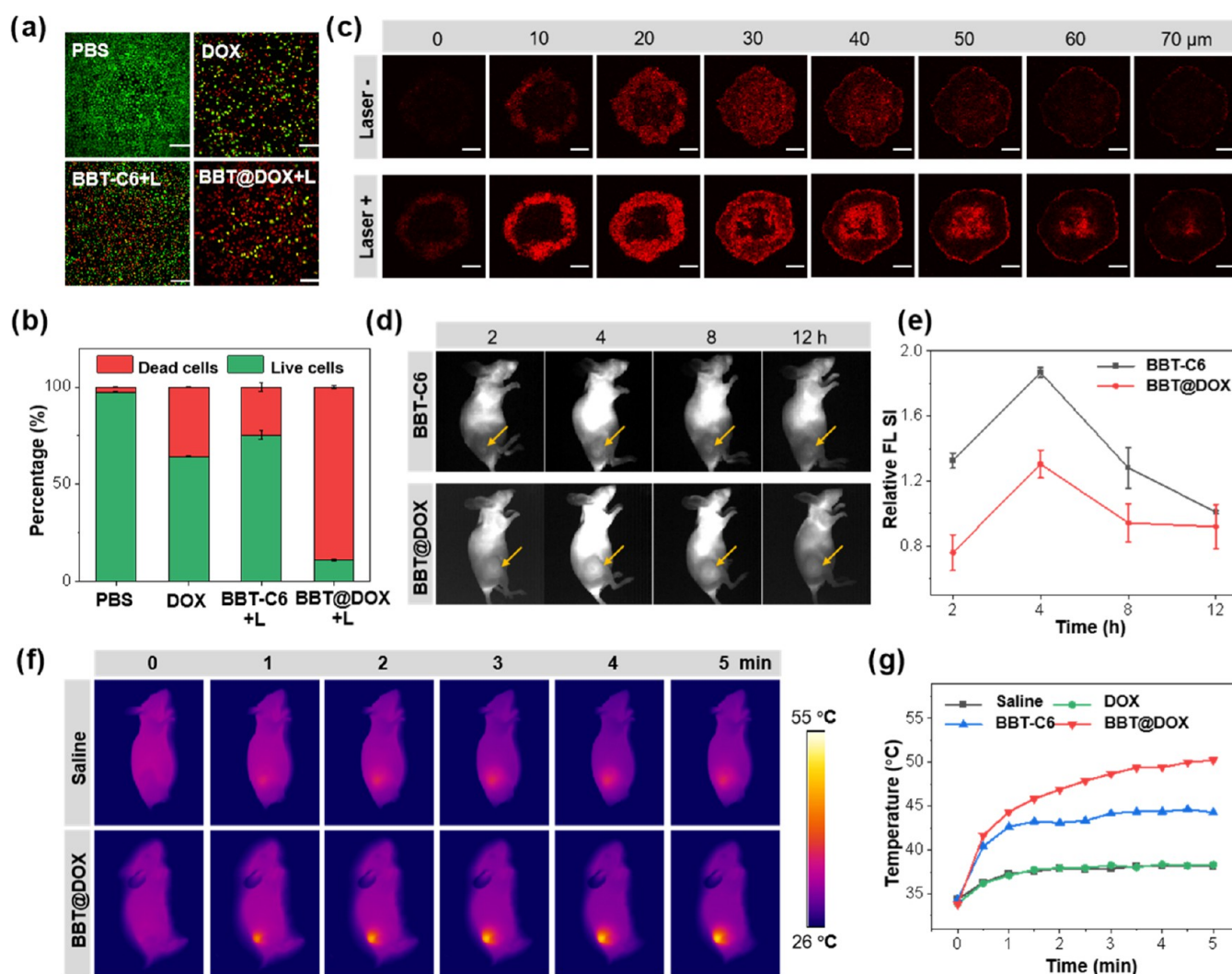
Figure 4. Calcein AM-PI double-staining of A549 cells with the indicated treatment (a, Scale bar: 200 μm) and their quantitative analysis (b). Microscopic images of **BBT@DOX**-teated A549 cell spheroids with the indicated laser condition and depth (c, Scale bar: 200 μm). Whole-body NIR-II FL images (d, 808 nm excitation, 1000 LP, 100 ms exposure time) and relative SI in the tumor regions (e), and photothermal images (f) and real-time infrared thermal images of (g) of BALB/c nude mice bearing xenograft A549 lung tumors after the indicated intravenous (i.v.) injection. 808 nm laser irradiation at 0.8 W/cm^2 was used. Data were expressed as means ± standard deviation (n = 3). The corresponding images for DOX and **BBT-C6** of Figure 4g can be found in the Supporting Information.

nificantly higher cytotoxicity against both A549 cells and A549/DOX cells. Significant cytotoxicity of **BBT@DOX** against A549 cells and A549/DOX cells after laser irradiation was observed even at low concentrations of 18 μM DOX and 15 μM **BBT-C6**, demonstrating the high efficacy of combined photothermal-chemo therapy, even against drug-resistant cells (Figures 3a and S7c). In addition, the half-maximal inhibitory concentration (IC$_{50}$) of **BBT@DOX** against A549 cells and A549/DOX cells in the dark was significantly lower than that of DOX (Figure 3b), especially for A549/DOX cells, indicating that **BBT@DOX** can effectively overcome drug resistance. The synergistic effect between DOX (chemotherapy) and **BBT-C6**+laser (photothermal therapy) was evaluated by the combination index (CI), which was calculated as 0.38 and 0.40 against A549 cells and A549/DOX cells, respectively, indicating a strong synergistic antiproliferative effect. Finally, the biocompatibility of **BBT@DOX** was evaluated by a hemolysis assay, which showed no apparent hemolysis (<5%) up to 100 μM of **BBT-C6** (Figure 3c). These observations demonstrated the high biocompatibility of **BBT-C6**, the ability

of **BBT@DOX** to overcome drug resistance, and the efficient synergistic photothermal-chemo therapy of **BBT@DOX**.

Since many factors contribute to drug resistance, such as decreased drug uptake, increased drug efflux, and altered drug targets,[53,54] the potential mechanism of **BBT@DOX** to overcome drug resistance was then investigated in cells using confocal microscopy. In both A549 cells and A549/DOX cells, a significantly higher FL intensity of DOX in the nucleus was found in **BBT@DOX**-treated cells than in DOX-treated cells, with a peak FL intensity at 12 h (Figures 3d−h and S7d−f), indicating the enhanced uptake of DOX in **BBT@DOX**-treated cells. To explore whether the DOX in the nucleus was in its molecular form (released from **BBT@DOX**) or still encapsulated within **BBT@DOX**, we prepared Cy5-labeled **BBT@DOX** (**Cy5/BBT@DOX**) using Cy5-DSPE-PEG2000. The fluorescence tracking revealed that, in both A549 and A549/DOX cells, the fluorescence of Cy5 and DOX localized similarly to free Cy5 and free DOX, with the fluorescence intensities increasing over time (Figure S7g,h). This confirmed that the DOX observed in the nucleus was released from
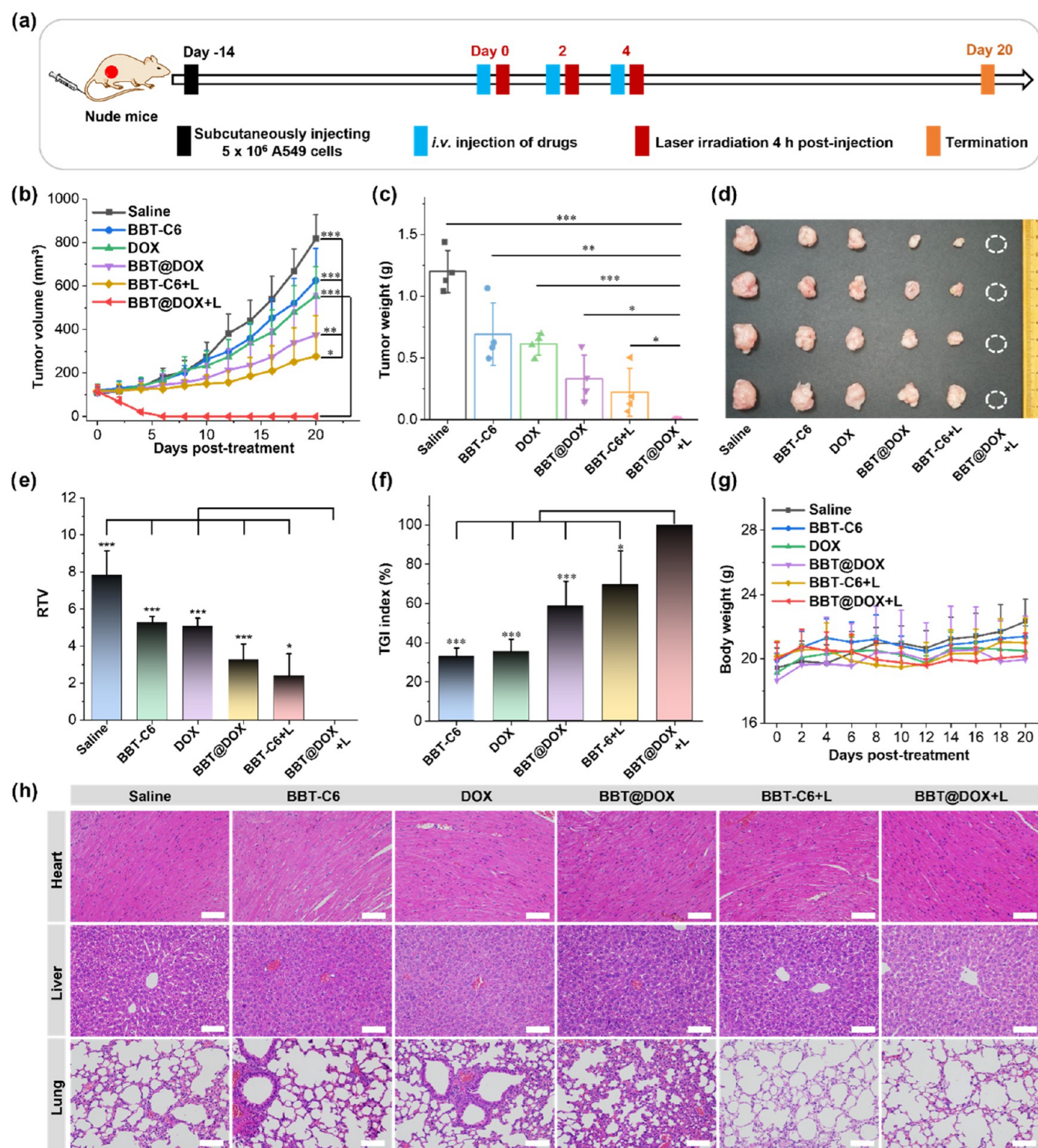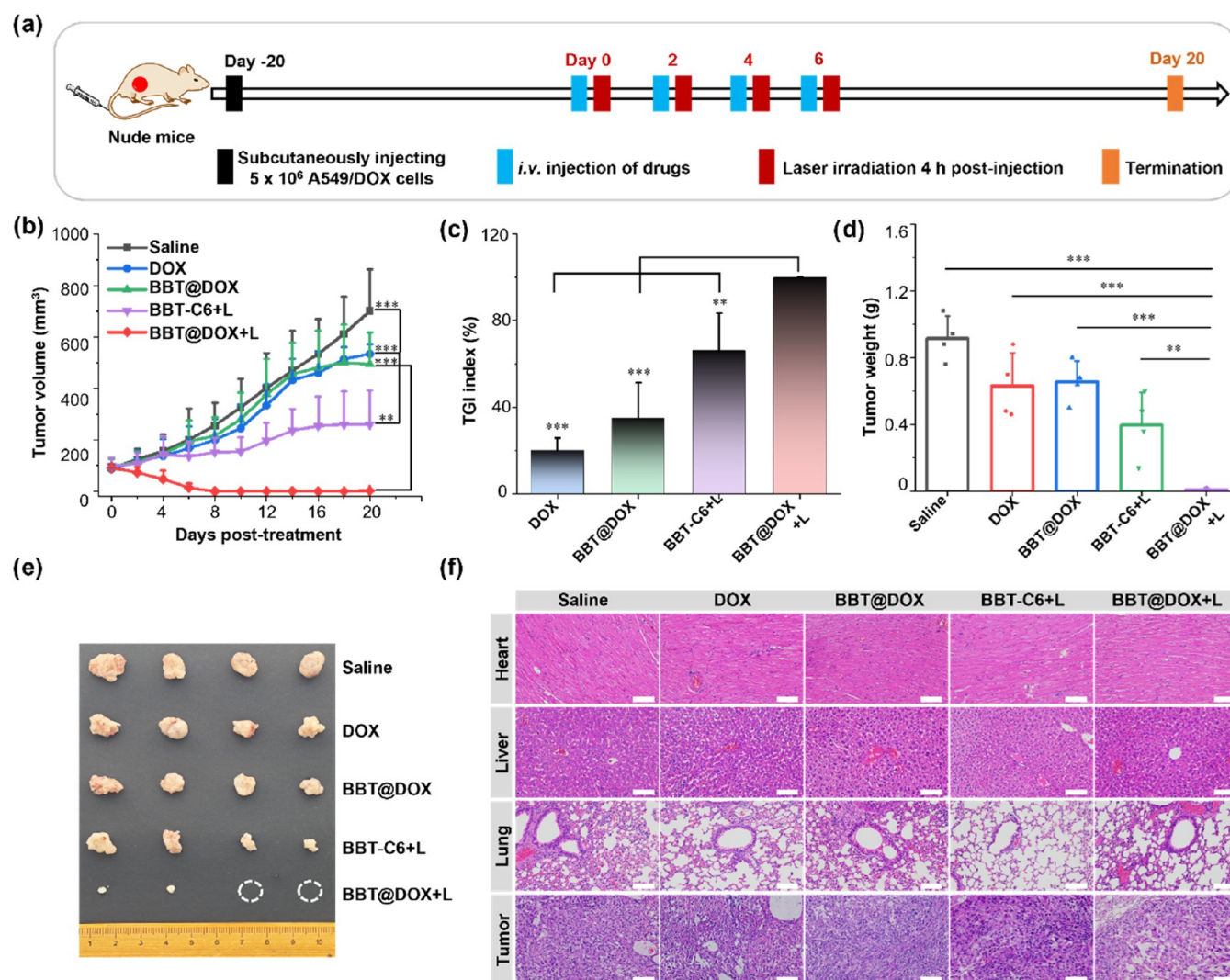
Figure 5. Schematic diagram of the therapeutic schedules (a). Tumor growth curves (b) of the treatment groups. Weight (c) and photos (d) of tumors collected after the treatments. RTV (e), TGI index (f), and body weight curves (g) of the treatment groups. H&E staining of internal organs from the treatment groups (h, scale bar: 100 μm). Data were presented as mean $\pm$ standard deviation ($n = 4$, the asterisks indicate the statistical significance, $*p < 0.05$, $**p < 0.01$, and $***p < 0.001$). 808 nm laser irradiation at 0.8 W/cm^2 was used.

BBT@DOX after internalization, rather than remaining encapsulated.

In DOX-treated A549/DOX cells, DOX initially accumulated in the nucleus but was subsequently effluxed, leading to a low nuclear fluorescence intensity at 12 h (Figure 3d,e). In contrast, high FL intensity of DOX remained in the nucleus of **BBT@DOX**-treated A549/DOX cells during this period

(Figure 3f,g). Notably, apparent nucleus dissociation was observed in **BBT@DOX**-treated A549/DOX cells, in contrast to the more intact nuclei seen in DOX-treated cells (Figure 3e,g). Quantitative analysis of confocal microscope images showed that the uptake of DOX in **BBT@DOX**-treated A549 and A549/DOX cells was 1.9- and 2.3-fold higher, respectively, than in DOX-treated cells at 12 h (Figures 3h and S7f). This

Figure 6. Schematic diagram of the therapeutic schedules (a). Tumor growth curves (b), TGI index (c) of the treatment groups. Weight (d) and photos (e) of tumors collected after the treatments. H&E staining of internal organs and tumors from the treatment groups (f, scale bar: 100 μm). Data were presented as mean $\pm$ standard deviation ($n = 4$, the asterisks indicate the statistical significance, $*p < 0.05$, $**p < 0.01$, and $***p < 0.001$). 808 nm laser irradiation at 0.8 W/cm^2 was used.

demonstrated that **BBT@DOX** could effectively enhance cellular uptake of DOX.

To further elucidate the mechanism by which **BBT@DOX** overcome drug resistance, we first examined the expression of a key drug resistance-related protein P-glycoprotein (P-gp), which acts as an adenosine triphosphate (ATP)-powered efflux pump.[55] The results confirmed that P-gp was overexpressed in A549/DOX cells (Figure 3i). After coincubating A549/DOX cells with DOX, **BBT-C6**, or **BBT@DOX**, no significant changes in P-gp expression were observed (Figure 3i), suggesting that **BBT@DOX** does not overcome drug resistance by directly inhibiting P-gp. Subsequent A549/DOX cellular uptake studies with varying concentrations of DOX and **BBT@DOX** were conducted. The results showed that the uptake of both DOX and **BBT@DOX** increased with higher concentrations (Figure 3j–l), highlighting the limited efflux capacity of A549/DOX cells when intracellular concentrations are elevated. Owing to its small particle size (67 nm), **BBT@DOX** could be efficiently taken up by cells.[56] Once internalized, **BBT@DOX** rapidly releases DOX, leading to increased intracellular DOX concentrations. This increased

accumulation of DOX exceeds the efflux capacity of A549/DOX cells, thereby enabling **BBT@DOX** to effectively overcome drug resistance.[57]

2.4. Tumor Penetration, In Vivo NIR-II FLI, and Photothermal Efficacy of BBT@DOX. Next, the therapeutic efficacy of **BBT@DOX** was evaluated by live−dead cell double-staining experiments and cell spheroid models. In A549 cells treated with DOX or **BBT-C6**+laser, weak red FL of propidium iodide (PI) from dead cells and strong green FL of Calcein AM from live cells were detected. Quantitative analysis revealed only 36 and 25% cell death caused by DOX or **BBT-C6**+laser, respectively, indicating the low therapeutic efficacy of chemotherapy or PTT alone. In contrast, intense red FL from dead cells was detected in **BBT@DOX**+laser-treated A549 cells with approximately 89% cell death (Figure 4a,b), highlighting the high efficacy of synergistic photothermal-chemo therapy. The results were in good agreement with the cytotoxicity assay findings. Since poor tumor penetration of drug delivery systems prevents effective drug delivery to the center of the tumor and increases the risk of drug resistance, three-dimensional (3D) A549 cell spheroid models were

cultured to investigate the tumor penetration behavior of **BBT@DOX**, which simulates the high cell density, dense extracellular matrix, and high interstitial pressure of tumor tissues. Without 808 nm laser irradiation, confocal microscope images of **BBT@DOX**-treated A549 cell spheroids showed weak red FL of DOX in the peripheral region and negligible red FL in the central region above the depth of 40 μm. In contrast, a significantly stronger red FL of DOX was found in the **BBT@DOX**+laser-treated A549 cell spheroids (Figure 4c). Moreover, intense red FL of DOX was found in the central region even at 60 μm depth, showing that the photothermal effect dramatically promoted the penetration of DOX into the spheroids. Therefore, the photothermal effect of **BBT@DOX** significantly improved therapeutic efficiency by promoting the uptake and penetration of DOX, thus achieving effective photothermal-chemo therapy.

The in vivo NIR-II FL and photothermal efficacy of **BBT@DOX** were then evaluated in BALB/c nude mice bearing xenograft A549 lung tumors. Prior to the imaging study, acute toxicity was evaluated in three BALB/c nude mice by intravenous (i.v.) injection of **BBT@DOX** at a **BBT-C6** dose of 5 mg/kg, which showed no signs of toxicity or tissue abnormalities. The NIR-II FL images of mice after i.v. injection of **BBT-C6** and **BBT@DOX** demonstrated higher in vivo imaging and tumor targeting capabilities of **BBT@DOX** (Figure 4d, $n = 3$), resulting in much higher NIR-II FL signal intensity (SI) in the tumor region with a peak SI at 4 h postinjection (Figures 4e and S8). Thermal images of mice after i.v. injection of **BBT@DOX** at a **BBT-C6** dose of 5 mg/kg showed a dramatic temperature increase to 50 °C in the tumor region after 5 min of 808 nm laser irradiation at a power of 0.8 W/cm^2, sufficient for photothermal therapy. In contrast, mice treated with **BBT-C6** showed a moderate temperature increase to 44 °C, and those treated with saline or DOX exhibited a minimal increase to 38 °C (Figures 4f,g and S9). Therefore, the high in vivo biocompatibility, NIR-II FL imaging capability, and photothermal efficacy demonstrated the high potential of **BBT@DOX** for NIR-II FL imaging-guided photothermal-chemo therapy in mice.

2.5. Chemo-Photothermal Therapy of Xenograft A549 and A549/DOX Lung Cancer with BBT@DOX.

Finally, the chemo-PTT efficacy of **BBT@DOX** was investigated in six groups of BALB/c nude mice bearing xenograft A549 lung tumors ($n = 4$). When the tumor volume reached 100−150 mm^3, the mice were i.v. injected with saline, DOX, **BBT-C6** (two groups), and **BBT@DOX** (two groups) every 2 days, for a total of three injections (Figure 5a). Based on the peak NIR-II FL signal intensity in the tumor region (Figure 4d,e), two groups of mice treated with **BBT-C6** and **BBT@DOX** were exposed to an 808 nm laser at 0.8 W/cm^2 for 5 min at 4 h postinjection. The tumor growth curve (Figure 5b), along with tumor weight (Figure 5c), and photos (Figure 5d) collected on day 21, demonstrated the high efficacy of the **BBT@DOX**+laser treatment, with tumors nearly eradicated. To assess the therapeutic efficacy, relative tumor volume (RTV) and the tumor growth inhibition index (TGI, <50% considered as nonresponse) were determined (Figure 5e,f). Negligible efficacy was observed in the DOX and **BBT-C6** treatment groups (TGI < 50%), likely due to the low DOX dose (1 mg/kg) and the low dark toxicity of **BBT-C6**. The higher TGI (>50%) in the **BBT@DOX** and **BBT-C6**+laser treatment groups indicated improved therapeutic efficacy due to the formulation and PTT, respectively. In the **BBT@DOX**

+laser treatment group, a low RTV of 0% and a high TGI of 100% highlighted the effectiveness of the combined therapy, even at low doses of DOX (1 mg/kg) and **BBT-C6** (5 mg/kg). Benefiting from the low doses, no signs of toxicity or notable weight loss were observed in the treatment groups (Figure 5g). In addition, histological hematoxylin and eosin (H&E) staining of internal organs collected after therapy showed no abnormalities associated with **BBT-C6** or **BBT@DOX** treatment (Figure 5h and S10). Therefore, high chemo-PTT efficacy was achieved by the **BBT@DOX**+laser treatment of mice with statistical significance.

The promising therapeutic efficacy encouraged us to investigate the potential of **BBT@DOX** in treating drug-resistant A549/DOX xenograft tumors. When the tumor volume reached 100 mm^3, five groups of mice ($n = 4$) were i.v. injected with saline, DOX, **BBT-C6**, and **BBT@DOX** (two groups) every 2 days for a total of four injections, respectively (Figure 6a). The **BBT-C6** group and one of the **BBT@DOX** groups were irradiated with an 808 nm laser at 0.8 W/cm^2 for 5 min at 4 h postinjection. The DOX and **BBT@DOX** groups exhibited relatively low tumor inhibition, with TGI indexes of 20.0 and 34.9%, respectively, while in the A549 tumor model, the values were slightly higher at 35.5 and 58.6%. A significance analysis of these differences revealed that the DOX group showed a statistically significant difference in therapeutic effect between the two tumor models ($p = 0.02$), while the **BBT@DOX** group did not display a significant difference ($p = 0.08$) (Figure S11a). This suggests that the A549/DOX tumors have developed resistance to DOX treatment, but exhibit lower resistance to **BBT@DOX**. Fortunately, the **BBT@DOX**+laser group demonstrated a highly effective therapeutic outcome, achieving a TGI index of 99.7% and successfully overcoming the drug resistance (Figure 6b,c), confirmed by tumors harvested on day 21 (Figure 6d,e). Notably, the **BBT-C6**+laser group also showed moderate efficacy, with a TGI index of 66.0%, indicating the potential for drug-resistant free PTT (Figure 6b,c). Due to the low laser power and short irradiation time, no signs of burns were observed at the original tumor site (Figure S11b). No apparent body weight loss was observed in any of the groups throughout the therapy (Figure S11c), indicating the high biosafety of these treatments. Meanwhile, neither significant organ damage nor inflammation was observed in hematoxylin and eosin (H&E) staining images of major organs collected from the treatment groups (Figures 6f and S11d), further demonstrating high biosafety. In contrast, obvious necrosis was observed in the tumor sections from the **BBT@DOX**+laser treatment group, as indicated by H&E staining (Figure 6f). Therefore, the chemo-PTT with **BBT@DOX** effectively overcame drug resistance, offering a promising strategy for the treatment of drug-resistant A549/DOX lung cancer. However, the laser power intensity used for treatment (0.8 W/cm^2) is relatively high and may pose challenges for clinical translation. Moving forward, we aim to enhance the PCE of BBTD-based amphiphilic dyes to facilitate safer and more effective clinical applications.

3. CONCLUSIONS

In conclusion, our study demonstrated the successful development and application of a Janus macromolecular amphiphilic NIR-II fluorophore as an all-in-one "add-on" module for convenient multifunctionalization of theranostics for NIR-II FLI-guided synergistic chemo-photothermal therapy of drug-

resistant lung cancer. The introduction of amphiphilic side chains containing OEG and hexyl chains into the planar D−A−D core achieves a delicate balance between NIR-II fluorescence and photothermal effect, endowing the BBTD-based fluorophore **BBT-C6** with AIE characteristics, moderate PCE (37.9% under 808 nm irradiation), good water solubility, and robust photostability. With a favorable Log P value of 1.61 and a low CMC of 15.4 μM, **BBT-C6** could self-assemble as an "add-on" module onto DOX-loaded nanoparticles, providing multifunctionalized, monodisperse, stable, and biocompatible nanoparticles **BBT@DOX**. This approach simplifies the drug delivery system by replacing multiple components, such as NIR-II fluorophore, photothermal agent, and PEGylation agents, with just one module. Moreover, the rapid accumulation of **BBT@DOX** at the tumor site, peaking at 4 h postinjection, which may be attributed to its small particle size of approximately 67 nm, is good for patient compliance. The ability and potential mechanism of **BBT@DOX** to overcome drug resistance was demonstrated by the findings that **BBT@DOX** has a lower IC_{50}, significant higher cellular uptake, and deeper penetration into tumor spheroids compared to DOX. Both in vitro and in vivo experiments suggest that **BBT@DOX** enables effective chemo-photothermal synergistic therapy against DOX-resistant lung cancer, as evidenced by a CI of 0.40 and complete tumor eradication at a low DOX dose of 1 mg/kg. While the efficacy of combination therapy based on a single nanosystem is widely recognized, the complexity of the nanosystem remains an unavoidable bottleneck for its clinical development. The all-in-one "add-on" module developed herein offers a standardized "on-call" module for the rapid construction of anticancer theranostics, effortlessly equipping regular nanoparticles with attractive NIR II-FLI, PEGylation, and PTT functions, and thus providing a useful strategy for the development of advanced NIR-II and photothermal theranostics.

4. EXPERIMENTAL PROCEDURE

4.1. Synthesis and Characterization of BBT-Base Fluorophores. Take the synthesis of **BBT-OEG** as an example. Under a nitrogen atmosphere, compound **7a** (1.0 g, 0.7 mmol) and 4,8-Dibromobenzo[1,2-*c*:4,5-*c*′]bis([1,2,5]thiadiazole) (96.0 mg, 0.3 mmol) were dissolved in 30 mL of 1,4-dioxane and 6 mL of 1 M potassium acetate aqueous solution (1,4-dioxane/H$_2$O = 5:1). Pd(dppf)Cl$_2$ (48 mg, 65.6 μmol) was then added to the mixture, the resulting reaction mixture was stirred at 80 °C. Upon completion of the reaction as indicated by thin layer chromatography, the mixture was extracted with CH$_2$Cl$_2$, and the organic phase was dried, filtered, and purified by reversed-phase silica gel column chromatography (MeOH: H$_2$O = 19:1) to provide **BBT-OEG** as a blue wax (245.0 mg, 30% yield). ^{1}H NMR (500 MHz, Chloroform-*d*) δ 8.14 (d, J = 8.7 Hz, 4H), 7.19 (d, J = 8.9 Hz, 8H), 7.12 (d, J = 8.5 Hz, 8H), 6.90 (d, J = 8.9 Hz, 8H), 4.49 (s, 8H), 3.66−3.60 (m, 160H), 3.57−3.52 (m, 16H), 3.36 (s, 12H). ^{13}C NMR (126 MHz, Chloroform-*d*) δ 168.2, 154.0, 152.7, 148.7, 141.4, 132.7, 127.5, 127.3, 120.0, 119.6, 115.9, 71.9, 70.6, 70.6, 70.5, 70.3, 69.8, 67.8, 59.0, 38.8. MS (MALDI-TOF) m/z: [M + Na]$^+$ calcd for C$_{142}$H$_{224}$N$_{10}$NaO$_{52}$S$_2$$^+$ 2988.453; found 2987.118.

4.2. Preparation of BBT@DOX and BBT-Cy5@DOX. The nanoemulsions were prepared by the thin-film dispersion method, using soybean phospholipid S95 and Pluronic F68 as surfactants. Briefly, 20 mg of S95, 2 mg of **BBT-C6**, and 0.4 mg of DOX were dissolved in 2 mL of MeOH. Removal of MeOH under vacuum provided a thin lipid film, and then 2 mL of an aqueous solution containing F68 (20 mg) was added. After 10 min of ultrasound treatment, the mixture underwent further processing with a cell

disruptor for 5 min (3 s on, 3 s off cycle, at 40% power), followed by filtration through a 220 nm membrane to provide **BBT@DOX**.

BBT-Cy5@DOX was prepared according to the method for **BBT@DOX**, with the addition of 1 mg of Cy5-DSPE-PEG2000 before the formation of the thin film.

4.3. Evaluation of Dox Encapsulation Efficiency and Drug Loading Content. Encapsulation efficiency (EE%) and drug loading content (DLC%) of **BBT@DOX** were determined using high-performance liquid chromatography (HPLC, Shimadzu LC-20A, an Amethyst C18−H reversed-phase column was used, particle size 5.0 μm, column dimension 4.6 × 250 mm^2). A calibration curve for doxorubicin (DOX) in methanol was first plotted using HPLC. Then, 100 μL of **BBT@DOX** was sonicated in 900 μL of methanol for 20 min and then centrifuged (12,000 rpm, 20 min). The DOX content in the supernatant was determined by HPLC as the total DOX content in nanoemulsions (W_t). Another 100 μL of the nanoemulsions **BBT@DOX** was diluted with H$_2$O and transferred to an ultrafiltration centrifuge tube (molecular weight cutoff 1 kDa). After centrifugation at 12,000 rpm for 20 min, methanol was added to dissolve the trapped nanoemulsions. The DOX content in the methanol solution was measured by HPLC to determine the encapsulated DOX content in **BBT@DOX** (W_o). EE% and DLC% were calculated using eqs 1 and 2, respectively, where W_d represents the weight of **BBT@DOX**.

$$EE\% = W_o/W_t \times 100\% \tag{1}$$

$$DLC\% = W_o/W_d \times 100\% \tag{2}$$

4.4. Cell Culture. The human lung adenocarcinoma cell line (A549) was purchased from Beyotime (Shanghai, China). Human normal lung epithelial cell line (BEAS-2B) was purchased from Wuhan Xavier Biotechnology Co., Ltd. Human lung adenocarcinoma cell/DOX-resistant strain A549/DOX was purchased from Shanghai Fuyu Biotechnology Co., Ltd. The cells were cultured in a cell incubator at 37 °C and 5% CO$_2$ using Dulbecco's modified eagle medium (DMEM) (high glucose) medium supplemented with 10% (v/v) fetal bovine serum and 1% (v/v) penicillin-streptomycin.

4.5. Cytotoxicity Assays. The cytotoxicity of **BBT-C6** and **BBT@DOX** against A549 and A549/DOX cells was evaluated using a cell counting kit assay (CCK-8, Beyotime, China). Taking A549 as an example, A549 cells were seeded in 96-well plates at an intensity of approximately 1.0×10^4 cells per well. After 24 h incubation, the medium was replaced with DMEM containing **BBT-C6**, DOX, or **BBT@DOX** at various concentrations (**BBT-C6** concentration: 3.8, 7.5, 15, 30, and 60 μM; DOX concentration: 1.8, 3.8, 7.5, 15, and 30 μM) and incubated for 12 h. Then, the medium was removed and the cells were washed with PBS (pH 7.4) three times. Fresh medium (0.1 mL) was added, and cells were further incubated for 12 h. For the laser treatment groups, cells were exposed to an 808 nm laser at an energy density of 1.0 W/cm^2 for 10 min. Then, 0.1 mL of CCK-8 was added to each well. After 1−3 h of incubation, the optical density (OD) at 450 nm was measured using a microplate reader (BIO-RAD 550).

4.6. Cellular Uptake of BBT@DOX. A549 and A549/DOX cells were seeded into 20 mm confocal dishes at a density of 2×10^5 cells per dish. After 24 h of adherent culture, the old medium was removed. DMEM containing DOX or **BBT@DOX** (DOX concentration: 4 μg/mL) was added and incubated for 1, 4, 6, and 12 h, respectively. Subsequently, the culture medium was carefully discarded, and the cells were washed with PBS (pH 7.4). The cells were then fixed with 4% paraformaldehyde for 15 min, followed by three washes with PBS. Next, the cells were stained with 200 μL DAPI for 10 min and washed six times with PBS. The cellular uptake of DOX and **BBT@DOX** was studied by laser scanning confocal microscopy (A1R/A1, Nikon).

4.7. 3D A549 Cell Spheroid Model. Agarose hydrogel (1.5%, 50 μL) was added to each well of a 96-well culture plate, ensuring complete coverage of the well bottom and forming a suitable concave shape upon addition. The plates were then incubated at 37 °C for 2 h, and A549 cells were seeded at a density of 2×10^4 cells per well in 200 μL of DMEM. Plates were further incubated at 37 °C for 3−5 days to allow the formation of 3D spheroids in culture. Once the

tumor spheroids reached approximately 100 μm in size, a DMEM containing **BBT@DOX** (DOX concentration: 16 μg/mL, **BBT-C6** concentration: 60 μM) was added and coincubated for 4 h. For the laser treatment group, cells were irradiated with an 808 nm laser at a power of 1.0 W/cm^2 for 10 min. After treatment, the tumor spheroids were washed with PBS, transferred into a 20 mm confocal dish, and fixed with 4% paraformaldehyde for 30 min. Subsequently, cross-sectional images of the tumor spheroids were acquired at 10 μm intervals using laser scanning confocal microscopy.

4.8. Animals and Tumor Model. BALB/c female nude mice at 5−6 weeks old were purchased from Hubei BIONT Biological Technology Co., Ltd. (Hubei, China). All animal experiments strictly adhered to the Guideline for Animal Care and Use, Innovation Academy for Precision Measurement Science and Technology, Chinese Academy of Sciences (APM23042A). A xenograft tumor model was established in nude mice (female, 20 ± 2 g, 5−6 weeks old) by injecting either A549 cells (5 × 10^6 cells in 100 μL PBS) into the right hind flank. The length (L) and width (W) of each tumor were measured, and the tumor volume (V) was calculated using the following formula: $V = L \times W^2 \times 0.5$.

4.9. In Vivo NIR-II Fluorescence Imaging. When the tumor size reached approximately 200−300 mm^3, the mice were randomly divided into two groups ($n = 3$): **BBT-C6** and **BBT@DOX**. A 100 μL intravenous injection of **BBT-C6** or **BBT@DOX** was administered, with a dose of 1 mg/kg DOX and 5 mg/kg **BBT-C6**. Biodistribution of **BBT-C6** and **BBT@DOX** was imaged at 2, 4, 8, and 12 h postinjection using a near-infrared second window fluorescent imaging system (Series II 900/1700, NIROPTICS, China).

4.10. In Vivo Photothermal Efficacy. When the tumor size reached approximately 200−300 mm^3, the mice bearing A549 tumors were randomly divided into 4 groups: (1) saline, (2) DOX, (3) BBT-C6, (4) BBT@DOX. The mice in group 1 were intravenously injected with saline, the mice in group 2 were intravenously injected with DOX·HCl solution (DOX dosage: 1 mg/kg), the mice in group 3 were intravenously injected with **BBT-C6** solution (**BBT-C6** dosage: 5 mg/kg), and the mice in group 4 were intravenously injected with **BBT@DOX** (DOX dosage: 1 mg/kg, **BBT-C6** dosage: 5 mg/kg). Four hours after administration, NIR-II laser irradiation at 808 nm with a power of 0.8 W/cm^2 was applied to the mice. Real-time monitoring of the tumor site temperature in each group was performed using a near-infrared thermal imager during laser irradiation.

4.11. In Vivo Therapy. When the tumor volume reached about 100 mm^3, the mice bearing A549 tumors were randomly divided into 6 groups: (1) saline, (2) BBT-C6, (3) DOX, (4) BBT@DOX, (5) BBT-C6+Laser, (6) BBT@DOX+Laser, with 4 mice in each group. The mice in group 1 were intravenously injected with saline, the mice in groups 2 and 5 were intravenously injected with **BBT-C6** solution (**BBT-C6** dosage: 5 mg/kg), the mice in group 3 were intravenously injected with DOX·HCl solution (DOX dosage: 1 mg/kg), and the mice in groups 4 and 6 were intravenously injected with **BBT@DOX** (DOX dosage: 1 mg/kg, **BBT-C6** dosage: 5 mg/kg). On days 0, 2, and 4, the mice in each group received injections of 100 μL of the corresponding drugs. Four hours after administration, groups 5 and 6 underwent irradiation with an 808 nm near-infrared laser at a power of 0.8 W/cm^2 for 5 min. The weight and tumor volume of the nude mice were measured and recorded every 2 days. After 20 days of treatment, the mice were sacrificed, and the major organs and tumors were collected, fixed with 4% paraformaldehyde, embedded in paraffin, and sectioned for H&E staining.

Antitumor activity was evaluated by the relative tumor volume (RTV) and tumor growth inhibition (TGI). RTV was calculated based on the measured results: $RTV = V_t/V_0$ (V_t: the tumor volume on day 20, V_0: the tumor volume on day 0). TGI for each model was calculated as follows

$$TGI = \left(1 - \frac{RTV_T}{RTV_C}\right) \times 100\%$$

where RTV_T represents the mean RTV of the treatment group, and RTV_C represents the mean RTV of the saline group. The efficacy evaluation criteria were as follows: (a) response, >80% TGI; (b) stability, 50−80% TGI; and (c) nonresponse, <50% TGI.[58]

4.12. Statistical Analysis. The analyzed data are presented as mean ± standard deviation of $n \geq 3$ replicates unless otherwise stated. Statistical significance was assessed by unpaired t-test. Asterisks indicate significant differences: $p < 0.05$ was considered the probability threshold for statistical significance, *$p < 0.05$, **$p < 0.01$, ***$p < 0.001$.

■ ASSOCIATED CONTENT

ⓢ Supporting Information

The Supporting Information is available free of charge at https://pubs.acs.org/doi/10.1021/acsami.4c14519.

> Experimental materials; supplementary figures and tables; synthesis and characterization of the BBTD-base fluorophores; characterization of **BBT@DOX**; evaluation of photothermal properties; cell and animal studies; and copies of ^{1}H/^{13}C/^{19}F NMR and MS spectra of the BBTD-base fluorophores (PDF)

■ AUTHOR INFORMATION

Corresponding Authors

Zhong-Xing Jiang − *Innovation Academy for Precision Measurement Science and Technology, Chinese Academy of Sciences-Wuhan National Laboratory for Optoelectronics, Wuhan 430071, China; University of Chinese Academy of Sciences, Beijing 100049, China;* ⓞ orcid.org/0000-0003-2601-4366; Email: zxjiang@apm.ac.cn

Shizhen Chen − *Innovation Academy for Precision Measurement Science and Technology, Chinese Academy of Sciences-Wuhan National Laboratory for Optoelectronics, Wuhan 430071, China; University of Chinese Academy of Sciences, Beijing 100049, China;* Email: chenshizhen@apm.ac.cn

Authors

Yu Li − *Innovation Academy for Precision Measurement Science and Technology, Chinese Academy of Sciences-Wuhan National Laboratory for Optoelectronics, Wuhan 430071, China*

Qiang Zhu − *Innovation Academy for Precision Measurement Science and Technology, Chinese Academy of Sciences-Wuhan National Laboratory for Optoelectronics, Wuhan 430071, China; University of Chinese Academy of Sciences, Beijing 100049, China*

Pei He − *Innovation Academy for Precision Measurement Science and Technology, Chinese Academy of Sciences-Wuhan National Laboratory for Optoelectronics, Wuhan 430071, China*

Tingjuan Wu − *Innovation Academy for Precision Measurement Science and Technology, Chinese Academy of Sciences-Wuhan National Laboratory for Optoelectronics, Wuhan 430071, China*

Zhen Ouyang − *School of Pharmaceutical Sciences, Wuhan University, Wuhan 430071, China*

Lijun Zhu − *Innovation Academy for Precision Measurement Science and Technology, Chinese Academy of Sciences-Wuhan National Laboratory for Optoelectronics, Wuhan 430071, China*

Fang Wang − *Innovation Academy for Precision Measurement Science and Technology, Chinese Academy of Sciences-Wuhan*

National Laboratory for Optoelectronics, Wuhan 430071, China

Xin Zhou − *Innovation Academy for Precision Measurement Science and Technology, Chinese Academy of Sciences-Wuhan National Laboratory for Optoelectronics, Wuhan 430071, China; University of Chinese Academy of Sciences, Beijing 100049, China;* ◉ orcid.org/0000-0002-5580-7907

Complete contact information is available at:
https://pubs.acs.org/10.1021/acsami.4c14519

Author Contributions

‖Y.L., Q.Z., and P.H. contributed equally to this work.

Notes

The authors declare no competing financial interest.

■ ABBREVIATIONS

PTT, photothermal therapy; FLI, fluorescence imaging; ACQ, aggregation-caused fluorescence quenching; PCE, photothermal conversion efficiency; PEGylation, polyethylene glycolation; CMC, critical micelle concentrations

■ REFERENCES

(1) Liu, Y.; Bhattarai, P.; Dai, Z.; Chen, X. Photothermal Therapy and Photoacoustic Imaging via Nanotheranostics in Fighting Cancer. *Chem. Soc. Rev.* **2019**, *48*, 2053−2108.

(2) Chen, J.; Ning, C.; Zhou, Z.; Yu, P.; Zhu, Y.; Tan, G.; Mao, C. Nanomaterials as Photothermal Therapeutic Agents. *Prog. Mater. Sci.* **2019**, *99*, 1−26.

(3) Li, X.; Lovell, J. F.; Yoon, J.; Chen, X. Clinical Development and Potential of Photothermal and Photodynamic Therapies for Cancer. *Nat. Rev. Clin. Oncol.* **2020**, *17*, 657−674.

(4) Gao, M.; Yu, F.; Lv, C.; Choo, J.; Chen, L. Fluorescent Chemical Probes for Accurate Tumor Diagnosis and Targeting Therapy. *Chem. Soc. Rev.* **2017**, *46*, 2237−2271.

(5) Yin, X.; Cheng, Y.; Feng, Y.; Stiles, W. R.; Park, S. H.; Kang, H.; Choi, H. S. Phototheranostics for Multifunctional Treatment of Cancer with Fluorescence Imaging. *Adv. Drug Delivery Rev.* **2022**, *189*, No. 114483.

(6) Luo, H.; Gao, S. Recent Advances in Fluorescence Imaging-guided Photothermal Therapy and Photodynamic Therapy for Cancer: From Near-infrared-I to Near-infrared-II. *J. Controlled Release* **2023**, *362*, 425−445.

(7) Chen, H. J.; Wang, L.; Zhu, H.; Wang, Z. G.; Liu, S. L. NIR-II Fluorescence Imaging for *In Vivo* Quantitative Analysis. *ACS Appl. Mater. Interfaces* **2024**, *16*, 28011−28028.

(8) Meng, X.; Pang, X.; Zhang, K.; Gong, C.; Yang, J.; Dong, H.; Zhang, X. Recent Advances in Near-Infrared-II Fluorescence Imaging for Deep-Tissue Molecular Analysis and Cancer Diagnosis. *Small* **2022**, *18*, No. 2202035.

(9) Wang, F.; Zhong, Y.; Bruns, O.; Liang, Y.; Dai, H. In vivo NIR-II Fluorescence Imaging for Biology and Medicine. *Nat. Photonics* **2024**, *18*, 535−547.

(10) Li, C.; Chen, G.; Zhang, Y.; Wu, F.; Wang, Q. Advanced Fluorescence Imaging Technology in the Near-Infrared-II Window for Biomedical Applications. *J. Am. Chem. Soc.* **2020**, *142*, 14789−14804.

(11) Ding, Z.; Gu, Y.; Zheng, C.; Gu, Y.; Yang, J.; Li, D.; Xu, Y.; Wang, P. Organic Small Molecule-based Photothermal Agents for Cancer Therapy: Design Strategies from Single-molecule Optimization to Synergistic Enhancement. *Coord. Chem. Rev.* **2022**, *464*, No. 214564.

(12) Mu, J.; Xiao, M.; Shi, Y.; Geng, X.; Li, H.; Yin, Y.; Chen, X. The Chemistry of Organic Contrast Agents in the NIR-II Window. *Angew. Chem., Int. Ed.* **2022**, *61*, No. e202114722.

(13) Wang, R.; Li, X.; Yoon, J. Organelle-Targeted Photosensitizers for Precision Photodynamic Therapy. *ACS Appl. Mater. Interfaces* **2021**, *13*, 19543−19571.

(14) Zou, Q.; Bao, J.; Yan, X. Functional Nanomaterials Based on Self-Assembly of Endogenic NIR-Absorbing Pigments for Diagnostic and Therapeutic Applications. *Small Methods* **2022**, *6*, No. 2101359.

(15) Chang, R.; Zou, Q.; Zhao, L.; Liu, Y.; Xing, R.; Yan, X. Amino-acid-encoded Supramolecular Photothermal Nanomedicine for Enhanced Cancer Therapy. *Adv. Mater.* **2022**, *34*, No. 2200139.

(16) Cheng, P.; Pu, K. Activatable Phototheranostic Materials for Imaging-Guided Cancer Therapy. *ACS Appl. Mater. Interfaces* **2020**, *12*, 5286−5299.

(17) Xu, W.; Wang, D.; Tang, B. Z. NIR-II AIEgens: A Win-Win Integration towards Bioapplications. *Angew. Chem., Int. Ed.* **2021**, *60*, 7476−7487.

(18) Liu, Y.; Shen, G.; Zhao, L.; Zou, Q.; Jiao, T.; Yan, X. Robust Photothermal Nanodrugs Based on Covalent Assembly of Non-pigmented Biomolecules for Antitumor therapy. *ACS Appl. Mater. Interfaces* **2019**, *11*, 41898−41905.

(19) Zou, Q.; Abbas, M.; Zhao, L.; Li, S.; Shen, G.; Yan, X. Biological Photothermal Nanodots Based on Self-assembly of Peptide-Porphyrin Conjugates for Antitumor Therapy. *J. Am. Chem. Soc.* **2017**, *139*, 1921−1927.

(20) Liu, Y. S.; Wei, X.; Zhao, X.; Chen, L. J.; Yan, X. P. Near-Infrared Photothermal/Photodynamic-in-One Agents Integrated with a Guanidinium-Based Covalent Organic Framework for Intelligent Targeted Imaging-Guided Precision Chemo/PTT/PDT Sterilization. *ACS Appl. Mater. Interfaces* **2021**, *13*, 27895−27903.

(21) Nam, J.; Son, S.; Ochyl, L. J.; Kuai, R.; Schwendeman, A.; Moon, J. J. Chemo-photothermal Therapy Combination Elicits Anti-tumor Immunity Against Advanced Metastatic cancer. *Nat. Commun.* **2018**, *9*, No. 1074.

(22) Xu, C.; Pu, K. Second Near-infrared Photothermal Materials for Combinational Nanotheranostics. *Chem. Soc. Rev.* **2021**, *50*, 1111−1137.

(23) Huang, X.; Lu, Y.; Guo, M.; Du, S.; Han, N. Recent Strategies for Nano-based PTT Combined with Immunotherapy: From a Biomaterial Point of View. *Theranostics* **2021**, *11*, 7546−7569.

(24) Zhang, L.; Zhang, Y.; Xue, Y.; Wu, Y.; Wang, Q.; Xue, L.; Su, Z.; Zhang, C. Transforming Weakness into Strength: Photothermal-Therapy-Induced Inflammation Enhanced Cytopharmaceutical Chemotherapy as a Combination Anticancer Treatment. *Adv. Mater.* **2018**, *31*, No. 1805936.

(25) Qing, G.; Zhao, X.; Gong, N.; Chen, J.; Li, X.; Gan, Y.; Wang, Y.; Zhang, Z.; Zhang, Y.; Guo, W.; et al. Thermo-responsive Triple-function Nanotransporter for Efficient Chemo-photothermal Therapy of Multidrug-resistant Bacterial Infection. *Nat. Commun.* **2019**, *10*, No. 4336.

(26) Wang, L.; Yu, Y.; Wei, D.; Zhang, L.; Zhang, X.; Zhang, G.; Ding, D.; Xiao, H.; Zhang, D. A Systematic Strategy of Combinational Blow for Overcoming Cascade Drug Resistance via NIR-Light-Triggered Hyperthermia. *Adv. Mater.* **2021**, *33*, No. 2100599.

(27) Choe, H. S.; Shin, M. J.; Kwon, S. G.; Lee, H.; Kim, D. K.; Choi, K. U.; Kim, J. H.; Kim, J. H. Yolk-Shell-Type Gold Nanoaggregates for Chemo- and Photothermal Combination Therapy for Drug-Resistant Cancers. *ACS Appl. Mater. Interfaces* **2021**, *13*, 53519−53529.

(28) Chen, Y.; Chen, S.; Yu, H.; Wang, Y.; Cui, M.; Wang, P.; Sun, P.; Ji, M. D-A Type NIR-II Organic Molecules: Strategies for the Enhancement Fluorescence Brightness and Applications in NIR-II Fluorescence Imaging-Navigated Photothermal Therapy. *Adv. Healthcare Mater.* 2022, *11*, No. 2201158.

(29) Manivasagan, P.; Joe, A.; Han, H.-W.; Thambi, T.; Selvaraj, M.; Chidambaram, K.; Kim, J.; Jang, E.-S. Recent Advances in Multifunctional Nanomaterials for Photothermal-enhanced Fenton-based Chemodynamic Tumor Therapy. *Mater. Today Bio.* 2022, *13*, No. 100197.

(30) Zhang, J.; Liu, W.; Liu, Y.; Zhang, J.; Gao, P.; Zheng, L.; Xu, F.; Jin, G.; Tang, B. Z. A New Strategy to Elevate Absorptivity of AIEgens for Intensified NIR-II Emission and Synergized Multimodality Therapy. *Adv. Mater.* 2023, *35*, No. 2306616.

(31) Liu, L.; Wang, X.; Wang, L. J.; Guo, L.; Li, Y.; Bai, B.; Fu, F.; Lu, H.; Zhao, X. One-for-All Phototheranostic Agent Based on Aggregation-Induced Emission Characteristics for Multimodal Imaging-Guided Synergistic Photodynamic/Photothermal Cancer Therapy. *ACS Appl. Mater. Interfaces* 2021, *13*, 19668−19678.

(32) Zhu, J.; Zhang, H.; Chen, K.; Li, Y.; Yang, Z.; Chen, S.; Zheng, X.; Zhou, X.; Jiang, Z. X. Peptidic Monodisperse PEG "Comb" as Multifunctional "Add-On" Module for Imaging-Traceable and Thermo-Responsive Theranostics. *Adv. Healthcare Mater.* 2019, *9*, No. 1901331.

(33) Zhu, L.; Li, Y.; Jiang, M.; Ke, C.; Long, H.; Qiu, M.; Zhang, L.; Ye, C.; Zhou, X.; Jiang, Z. X.; Chen, S. Self-Assembly of Precisely Fluorinated Albumin for Dual Imaging-Guided Synergistic Chemo-Photothermal-Photodynamic Cancer Therapy. *ACS Appl. Mater. Interfaces* 2023, *15*, 2665−2678.

(34) Zhang, L.; Liu, Y.; Huang, H.; Xie, H.; Zhang, B.; Xia, W.; Guo, B. Multifunctional Nanotheranostics for Near Infrared Optical Imaging-guided Treatment of Brain Tumors. *Adv. Drug Delivery Rev.* 2022, *190*, No. 114536.

(35) Li, Y.; Zhang, J.; Zhu, L.; Jiang, M.; Ke, C.; Long, H.; Lin, R.; Ye, C.; Zhou, X.; Jiang, Z. X.; Chen, S. All-in-One Heptamethine Cyanine Amphiphiles for Dual Imaging-Guided Chemo-Photodynamic-Photothermal Therapy of Breast Cancer. *Adv. Healthcare Mater.* 2023, *12*, No. 2300941.

(36) Saikia, I.; Borah, A. J.; Phukan, P. Use of Bromine and Bromo-Organic Compounds in Organic Synthesis. *Chem. Rev.* 2016, *116*, 6837−7042.

(37) Minami, H.; Otsuka, S.; Nogi, K.; Yorimitsu, H. Palladium-Catalyzed Borylation of Aryl Sulfoniums with Diborons. *ACS Catal.* 2018, *8*, 579−583.

(38) Kadu, B. S. Suzuki-Miyaura Cross Coupling Reaction: Recent Advancements in Catalysis and Organic Synthesis. *Catal. Sci. Technol.* 2021, *11*, 1186−1221.

(39) Mohsen-Nia, M.; Ebrahimabadi, A. H.; Niknahad, B. Partition Coefficient n-octanol/water of Propranolol and Atenolol at Different Temperatures: Experimental and Theoretical studies. *J. Chem. Thermodyn.* 2012, *54*, 393−397.

(40) Ray, G. B.; Chakraborty, I.; Moulik, S. P. Pyrene Absorption can be a Convenient Method for Probing Critical Micellar Concentration (cmc) and Indexing Micellar Polarity. *J. Colloid Interface Sci.* 2006, *294*, 248−254.

(41) Deming, T. J. Synthesis of Side-Chain Modified Polypeptides. *Chem. Rev.* 2016, *116*, 786−808.

(42) Moro, S.; Siemons, N.; Drury, O.; Warr, D. A.; Moriarty, T. A.; Perdigão, L. M. A.; Pearce, D.; Moser, M.; Hallani, R. K.; Parker, J.; et al. The Effect of Glycol Side Chains on the Assembly and Microstructure of Conjugated Polymers. *ACS Nano* 2022, *16*, 21303−21314.

(43) Yao, X.; Qi, C.; Sun, C.; Huo, F.; Jiang, X. Poly(ethylene glycol) Alternatives in Biomedical Applications. *Nano Today* 2023, *48*, No. 101738.

(44) Zheng, Y.; Li, Y.; Ke, C.; Duan, M.; Zhu, L.; Zhou, X.; Yang, M.; Jiang, Z.-X.; Chen, S. Jellyfish-inspired Smart Tetraphenylethene Lipids with Unique AIE Fluorescence, Thermal Response, and Cell Membrane Interaction. *J. Mater. Chem. B* 2024, *12*, 2373−2383.

(45) Li, M.; Zhu, W.-H. Sterically Hindered Diarylethenes with a Benzobis(thiadiazole) Bridge: Enantiospecific Transformation and Reversible Photosuperstructures. *Acc. Chem. Res.* 2022, *55*, 3136−3149.

(46) Shen, H.; Sun, F.; Zhu, X.; Zhang, J.; Ou, X.; Zhang, J.; Xu, C.; Sung, H. H. Y.; Williams, I. D.; Chen, S.; et al. Rational Design of NIR-II AIEgens with Ultrahigh Quantum Yields for Photo- and Chemiluminescence Imaging. *J. Am. Chem. Soc.* 2022, *144*, 15391−15402.

(47) Wang, L.; Li, N.; Wang, W.; Mei, A.; Shao, J.; Wang, W.; Dong, X. Benzobisthiadiazole-Based Small Molecular Near-Infrared-II Fluorophores: From Molecular Engineering to Nanophototheranostics. *ACS Nano* 2024, *18*, 4683−4703.

(48) Ou, C.; Zhao, Z.; An, L.; Zheng, L.; Gao, F.; Zhu, Q.; Wang, W.; Shao, J.; Xie, L.; Dong, X. J-Aggregate Promoting NIR-II Emission for Fluorescence/Photoacoustic Imaging-Guided Phototherapy. *Adv. Healthcare Mater.* 2024, No. 2400846.

(49) Millard, M.; Bernhard, Y.; Canilho, N.; Grandemange, S.; Parant, S.; Mourer, M.; Lassalle, H.-P.; Pasc, A. Enhanced Stability and Photothermal Efficiency of Indocyanine Green J-aggregates by Nanoformulation with Calix[4]arene for Photothermal Therapy of Cancers. *Colloids Surf., B* 2023, *230*, No. 113516.

(50) Liu, S.; Zhou, X.; Zhang, H.; Ou, H.; Lam, J. W. Y.; Liu, Y.; Shi, L.; Ding, D.; Tang, B. Z. Molecular Motion in Aggregates: Manipulating TICT for Boosting Photothermal Theranostics. *J. Am. Chem. Soc.* 2019, *141*, 5359−5368.

(51) Li, S.; Deng, Q.; Zhang, Y.; Li, X.; Wen, G.; Cui, X.; Wan, Y.; Huang, Y.; Chen, J.; Liu, Z.; et al. Rational Design of Conjugated Small Molecules for Superior Photothermal Theranostics in the NIR-II Biowindow. *Adv. Mater.* 2020, *32*, No. 2001146.

(52) Wang, H.-X.; Zuo, Z.; Du, J.; Wang, Y.; Sun, R.; Cao, Z.; Ye, X.; Wang, J.; Leong, K. W.; Wang, J. Surface Charge Critically Affects Tumor Penetration and Therapeutic Efficacy of Cancer Nanomedicines. *Nano Today* 2016, *11*, 133−144.

(53) Kartal-Yandim, M.; Adan-Gokbulut, A.; Baran, Y. Molecular Mechanisms of Drug Resistance and Its Reversal in Cancer. *Criti. Rev. Biotechnol.* 2016, *36*, 716−726.

(54) Vasan, N.; Baselga, J.; Hyman, D. M. A View on Drug Resistance in Cancer. *Nature* 2019, *575*, 299−309.

(55) Kim, Y.; Chen, J. Molecular Structure of Human P-glycoprotein in the ATP-bound, Outward-facing Conformation. *Science* 2018, *359*, 915−919.

(56) Behzadi, S.; Serpooshan, V.; Tao, W.; Hamaly, M. A.; Alkawareek, M. Y.; Dreaden, E. C.; Brown, D.; Alkilany, A. M.; Farokhzad, O. C.; Mahmoudi, M. Cellular Uptake of Nanoparticles: Journey Inside the Cell. *Chem. Soc. Rev.* 2017, *46*, 4218−4244.

(57) Chen, H. L.; Liu, C. Y.; Yu, S. M.; Zhou, H. G.; Shafiq, F.; Qiao, W. H. Acid/GSH Dual-Responsive Endosome Escape Dual Pro-drug Micelles Targeted Synergistic Treatment for A549/ADR. *Langmuir* 2023, *39*, 7660−7671.

(58) Zhuo, J.; Lu, D.; Lin, Z.; Yang, X.; Yang, M.; Wang, J.; Tao, Y.; Wen, X.; Li, H.; Lian, Z.; et al. The Distinct Responsiveness of Cytokeratin 19-positive Hepatocellular Carcinoma to Regorafenib. *Cell Death Dis.* 2021, *12*, No. 1084.